PAPER

Check for updates

Resolving the organization of CO_2 molecules confined in silica nanopores using *in situ* small-angle neutron scattering and molecular dynamics simulations†

Sohaib Mohammed, [iD] Meishen Liu and Greeshma Gadikota [iD]*

Determining the organization of CO_2 molecules confined in nanoporous environments is essential for unlocking our understanding of the fate of CO_2 stored in nanoporous materials. In this study, we investigate the organization of pressurized CO_2 molecules in silica materials, MCM-41 and SBA-15 with cylindrical pore geometries and pore diameters of 3.3 nm and 6.8 nm, respectively at pressures ranging from vacuum to about 55 bar, using *in situ* small angle neutron scattering (SANS) measurements and classical molecular dynamics (MD) simulations. The nanoconfined CO_2 molecules are organized into core–shell structures with the shell resulting from CO_2 adsorption on the silica surfaces. The shell thicknesses of the adsorbed CO_2 molecules in MCM-41 pores obtained by SANS measurements are 0.7 ± 0.1 Å, 2.1 ± 0.1 Å, 2.2 ± 0.1 Å, 6.7 ± 0.1 Å, 11.5 ± 0.2 Å, and 12.6 ± 0.1 Å at equilibrated pressures of about 1.0, 14.9, 24.9, 34.7, 45.0 and 54.9 bar, respectively. The shell thicknesses of the adsorbed CO_2 molecules in SBA-15 pores are 2.2 ± 0.1, 2.9 ± 0.1, 5.1 ± 0.1, 8.8 ± 0.1, 12.4 ± 0.1, and 20.0 ± 0.1 at pressures of 0.9, 15.4, 24.9, 34.9, 45.0 and 55.5 bar, respectively. Close agreement between the experimental and MD simulations results are obtained. MD simulations also suggest that the adsorption of the CO_2 molecules is primarily driven by van der Waals interactions with minor contribution from the electrostatic interactions and hydrogen bonding with the surface hydroxyl groups. These findings inform the development of novel strategies to advance low carbon energy and resource recovery and to use and store CO_2 in natural and engineered materials.

Environmental significance

The societal need to transition to a sustainable low carbon energy and resource future requires rapid advancements in technologies to capture, convert, store, and remove CO_2 from our emissions. In this context, the ability to store CO_2 in geologic formations and in engineered porous materials is gaining increasing attention. One of the less studied but highly important consideration is the organization of confined CO_2 in nanoporous environments. A fundamental understanding of the organization of CO_2 molecules in nanoconfinement can unlock novel pathways for CO_2 separation or CO_2 storage in geologic and engineered materials. In this study, we investigate the organization of pressurized CO_2 molecules in silica materials, MCM-41 and SBA-15 with cylindrical pore geometries and pore diameters of 3.3 nm and 6.8 nm, respectively at pressures ranging from vacuum to about 55 bar, using small angle neutron scattering (SANS) measurements and classical molecular dynamics (MD) simulations. Our results reveal that the nanoconfined CO_2 molecules are organized into core–shell structures with the shell resulting from CO_2 adsorption on the silica surfaces. The shell thickness increased systematically with the applied pressure. We believe this paper is relevant to the field of low carbon energy and resource utilization technologies while achieving a stable and predictable climate on Earth. Thus, this study is a significant contribution to *Environmental Science: Nano*.

1. Introduction

The societal need to transition to a sustainable low carbon energy and resource future requires rapid advancements in

technologies to capture, convert, store, and remove CO_2 from our emissions. In this context, the ability to store CO_2 in geologic formations and in engineered porous materials for on-demand and distributed utilization is gaining increasing attention. One of the less studied but highly important considerations is the organization of confined CO_2 in nanoporous environments. Fluids confined in nanoporous environments have been shown to exhibit anomalous reactive behavior.[1–3] Anomalous reactive behaviors, particularly in

School of Civil and Environmental Engineering, Cornell University, Ithaca, NY 14853, USA. E-mail: gg464@cornell.edu; Tel: +1 607 255 4796
† Electronic supplementary information (ESI) available. See DOI: 10.1039/d0en01282c

2006 | *Environ. Sci.: Nano*, 2021, **8**, 2006–2018

This journal is © The Royal Society of Chemistry 2021

nanoconfined pores, influences our ability to predict the fate of CO_2 in geologic environments where CO_2 can mineralize to produce water insoluble calcium or magnesium carbonates.[4–6] In the context of engineered carbon removal, there is an emerging interest in harnessing nanoporous minerals and materials to store CO_2 as mineralized inorganic carbonates.[7–12] However, one of the more fundamental knowledge gaps that needs to be addressed is the organization of CO_2 in nanoporous media. Delineating the organization of nanoconfined CO_2 is essential to advance calibrated insights into the nano-scale reactivity of confined CO_2.

One of the less explored hypotheses associated with the transport and adsorption of solutes in pressurized CO_2 is the anomalous partitioning and reactivity due to the core–shell organization of pressurized CO_2 in confinement. With increasing interest in storing CO_2 in subsurface environments, predictions of multi-component ion transport and reactivity in these environments is limited by our understanding of the organization of confined CO_2. Further, there is interest in understanding how multiphase fluids are organized in nano-confinement in the context of long-term CO_2 storage, CO_2 utilization for heat mining, and for using pressurized CO_2 to extract organics in multiphase mixtures. To develop robust prediction capabilities associated with the fate and transport of CO_2 for these applications, the first step is to characterize the organization of pressurized CO_2 molecules in nanoconfinement. In this study, we investigate the organization of CO_2 molecules compressed in silica nanopores using small angle neutron scattering (SANS) measurements and classical molecular dynamics (MD) simulations.

The chemical interactions of CO_2 with solid interfaces have been investigated extensively in the context of the separation of CO_2 from multi-gas streams.[13–15] CO_2 adsorption and separation has been extensively investigated using a variety of porous sorbents such as carbonaceous materials,[16–18] zeolites,[19–21] alumina,[22] silica,[23,24] titania,[25] aerogels[26] and metal organic frameworks (MOFs).[27–29] Mesoporous silica-based sorbents have been widely utilized to selectively capture CO_2 from gaseous mixtures owing to the ease in tailoring their porous structure as well as the flexibility in tuning the surface chemistry by attaching different functional groups. Amine-incorporated mesoporous silica sorbents showed superior CO_2 uptake extents, high selectivity, high stability on adsorption/desorption performance and low energy requirements.[23,30] The outstanding performance of amine–silica composites stems from integrating the high CO_2 affinity of amines with large surface area of the mesoporous silica.

A wide range of characterization approaches were used to determine the performance of various silica-based sorbents for capturing CO_2. Experimental investigations of CO_2 capture in silica-based sorbents have been performed using X-ray diffraction (XRD),[30,31] neutron diffraction,[32] adsorption isotherms,[30] thermogravimetric analysis (TGA)[31] and Fourier transform infrared spectroscopy (FTIR).[33] In addition, different computational methods have been utilized to obtain

microscopic insights into CO_2–silica interfacial properties, including molecular dynamics (MD) simulations.[34–37] The design basis for developing novel sorbents for CO_2 capture has conventionally been the separation efficiency and the associated energy needs.[38–41] However, uncertainties associated with the molecular-scale organization of CO_2 molecules as a function of confinement and interfacial interactions in the context of CO_2 separation remain less studied.

Rising interest in storing acid gases in minerals motivated the investigation of the organization of these gases such as CO_2 and H_2S in porous minerals, clay minerals and silica.[35,42–47] These studies predicted the organization of acid gas molecules at solid interfaces and in confinement using classical MD simulations.[48–50] Compressed fluid storage in engineered and natural materials motivated the investigation of methane[51–54] hydrogen,[55–57] oxygen[58] and CO_2.[59]

The feasibility of experimentally validating molecular scale models predicting the organization of confined gases has been made possible by advancements in SANS measurements. Spatial resolution of the organization of confined fluids is possible using SANS measurements. For example, Melnichenko and co-workers[60] showed the formation of a dense adsorbed CO_2 phase in pores with diameters smaller than 4 nm at temperatures of 22 °C, 35 °C, and 60 °C in porous fractal silica using SANS measurements. The existence of two phases of CO_2 in silica aerogel nanopores at temperature range of 25–35 °C was also determined using SANS measurements.[61] Holewinski and co-workers[62] linked the CO_2 adsorption to the polymer morphology in poly(ethyleneimine)/mesoporous silica composites using SANS measurements, and showed an enhanced CO_2 capacity and uptake rates by the polymer supported on hydrophilic silica. Despite these advances, the following research questions remain unresolved in literature, and are therefore addressed in this study: (i) How does the organization of CO_2 in nano-confinement in silica nanopores change as a function of pressure? (ii) What is the level of agreement in the predictions and experiments of the organization of confined CO_2? (iii) What are the energetic interactions underlying the organization of confined CO_2 molecules?

To address these research questions, *in situ* SANS measurements of the organization of pressurized CO_2 molecules in mesoporous silica materials such as MCM-41 and SBA-15 mesoporous silica with pore diameters of 3.3 nm and 6.8 nm are probed at CO_2 pressures ranging from 0.93 bar to about 55 bars at ambient temperature. These experimental studies are complimented by classical MD simulations. The hypothesis that pressurized CO_2 molecules under confinement form core–shell structures with the shell arising from the adsorption of CO_2 on the pore surface is investigated. The findings from this study have implications for several applications associated with advancing low carbon energy recovery and utilization, and greenhouse gas storage.

In the context of storing CO_2 in depleted gas reservoirs, the organization of CO_2 and methane molecules in nanoconfined environments provides the basis for assessing the fate of these molecules and potential displacement of fluids or gases. The rising need to use anthropogenic CO_2 in distributed locations calls for developing novel engineered CO_2 storage materials. In this context, determining the organization of CO_2 in confinement and the ease of storing and recovering CO_2 from these materials is essential. The experimental and simulation methodologies described in this study facilitate the core–shell description of compressed confined fluids.

2. Methods

2.1. Small-angle neutron scattering measurements

The MCM-41 and SBA-15 mesoporous silica powders with pore diameters of 3.3 nm and 6.8 nm, respectively, were purchased from Sigma-Aldrich. The powders were degassed at 100 °C for 1.5 hours to remove the adsorbed water. 0.05 g of the degassed powder was then transferred to a special aluminum pressure cell with a diameter of 11 mm and a thickness of 1 mm. The effective thickness (L_{eff}) of the silica sample is less than the nominal thickness of the aluminum cell due to the presence of interparticle voids. The effective thickness of the silica powder is calculated as follows:

$$L_{eff} = L\frac{\rho_{bulk}}{\rho_{app}} \quad (1)$$

where L is the thickness of the aluminum cell, ρ_{bulk} is the bulk density which is the mass of the silica skeleton divided by the skeleton volume, pores volume and the volume of the interparticle voids, and ρ_{app} is the apparent density which is the mass of the silica skeleton divided by the skeleton volume and pores volume.[63]

CO_2 gas was injected to the powder and the neutron scattering intensities were collected at various pressures ranging from vacuum to about 55 bars in MCM-41 and SBA-15 samples (see Fig. 1(a)). The SANS measurements were performed at the 10 m SANS instrument at the National Institute of Standards and Technology (NIST), Center of Neutron Research (NCNR). The incident neutron beam has wavelengths (λ) of 5 Å and 12 Å, and the sample-to-detector distances (SSDs) were 1.2 m and 5.2 m to cover a wavevector (Q) range of 0.004 to 0.6 Å^{-1}. SANS data were corrected for the transmission, the background and the detector sensitivity.[64] The wavevector is $Q = \frac{4\pi}{\lambda}\sin\theta$, where λ is the incident beam wavelength and θ is half of the scattering angle (2θ). Further information on the SANS measurements and data analysis are included in Mohammed and co-workers.[51]

2.2. Classical molecular dynamics simulations

CO_2 and β-cristobalite silica unit cell were built using Avogadro software. The initial configurations of isolated cristobalite unit cell were optimized using density functional theory algorithm implemented in Quantum Espresso

Fig. 1 Schematic representation of the experimental setup for small-angle neutron scattering (SANS) measurements for determining the organization of confined CO_2 molecules in the pores of MCM-41 (pore diameter of 3.3 nm) and SBA-15 (pore diameter of 6.8 nm) silica materials is shown in (a). Snapshots of the simulated initial configurations showing CO_2 molecules and the simulated SBA-15 (top), and MCM-41 (bottom) silica pores are shown in (b). The atoms of silica pores and CO_2 molecules (see the color coding for the atoms below (b)) are drawn using VDW drawing method implemented in VMD software.

2008 | *Environ. Sci.: Nano*, 2021, **8**, 2006–2018

This journal is © The Royal Society of Chemistry 2021

software. The kinetic energy cutoff for wavefunctions and K-points mesh were converged based on the total energy values. The converged energy cutoff and K-points mesh were used to optimize the silica unit cell (see the initial and optimized unit cell coordinates in Fig. S1 and Table S1 in the ESI†). Ultrasoft pseudopotentials were used in which the generalized gradient approximation (GGA)[65,66] was selected for the exchange correlation functional. The structural optimization of the silica unit cell has been performed using the Broyden–Fletcher–Goldfarb–Shanno (BFGS) algorithm.

The optimized silica unit cell was replicated in x, y and z directions and MCM-41 and SBA-15 pores are cleaved in surfaces with dimensions of 77.96 Å × 76.43 Å × 39.8 Å and 124.45 Å × 152.85 Å × 49.78 Å in x, y, and z directions, respectively. Cylindrical-shaped pores with diameters of 3.32 nm and 6.83 nm were cleaved in the silica surfaces to mimic the MCM-41 and SBA-15 pores used in the SANS measurements (see Fig. 1(b)). The pore length of MCM-41 and SBA-15 are 3.54 nm and 4.98 nm, respectively. The nonbridging oxygens on the cleaved pore surfaces were protonated to achieve hydroxyl group density of about 8 OH per nm^2.[67,68] CO$_2$ molecules were distributed randomly in the pore space with the required number of molecules to match the pressure used in the SANS measurements. Silica surfaces were modeled using ClayFF forcefield.[69] CO$_2$ molecules were modeled using the forcefield developed by Potoff and Siepmann[70] (see Table 1 for the modeling parameters). The constructed simulation cells were set to be periodic in 3 dimensions.

The initial simulation cells were optimized using steepest descent energy minimization algorithm for 50 000 steps to eliminate the inappropriate geometries. NVT ensemble with a time step of 1 fs was performed on the optimized cells for 50 ns at 298 K using the Nosé–Hoover thermostat.[71,72] The bonded interactions are accounted for bonds stretching and angle bending in CO$_2$. Bond stretching in –OH groups in silica is also accounted for. The van der Waals and electrostatic nonbonded interactions were modeled by 12–6 Lennard-Jones and Coulomb's functions, respectively. The short range interactions were calculated within a cutoff of 14 Å, while long-range electrostatic interactions were modeled using particle mesh Ewald (PME).[73] GROMACS 2018 was used to perform and analyze the MD simulations.[74] VMD software were used for visualizing the simulation trajectories.[75] The

simulations were tested for equilibrium based on the potential energy profile of the system. The simulation was considered to reach equilibration once the potential energy profile become uniform and stable.

The structure of the adsorbed CO$_2$ on MCM-41 and SBA-15 pores was analyzed by calculating the thickness of the adsorbed layers (shell thickness) and the radial distribution function (g_{AB}). g_{AB} describes the density variations with the distance from a reference particle (r) as follow:

$$g_{AB}(r) = \frac{1}{\langle \rho_B \rangle_{local}} \frac{1}{N_A} \sum_{i \in A}^{N_A} \sum_{j \in B}^{N_B} \frac{\delta(r_{ij} - r)}{4\pi r^2} \quad (2)$$

in the expression above, ρ is the density and N_A is the number of A particles in the system.

3. Results and discussion

3.1. The adsorption of confined CO$_2$

The pressure dependent SANS intensities of CO$_2$ loaded MCM-41 and SBA-15 powders are depicted in Fig. 2. The intensity curves $I(Q)$ describe the influence of pressure on the form factor $[P(\vec{Q})]$ and the structure factor $[S(\vec{Q})]$ such that:

Table 1 Lennard-Jones parameters and the charges assigned to the silica and CO$_2$ atoms in the molecular dynamics simulations

Atom	σ (nm)	ε (kJ mol^{-1})	Charge (q)
Silica			
Si	0.3706	7.700×10^{-6}	+2.1000
O$_{bridging}$	0.3553	0.6502	−1.0500
O$_{hydroxyl}$	0.3353	0.6502	−0.9500
H$_{hydroxyl}$	0.0000	0.0000	+0.4250
CO$_2$			
C	0.2800	0.2245	+0.7000
O	0.3050	0.6569	−0.3500

Fig. 2 The small-angle neutron scattering intensities of CO$_2$-loaded (a) MCM-41 and (b) SBA-15 pores as a function of the wavevector and the applied pressure are shown. The insets represent the power law slope values as a function of the applied pressure.

$$I(Q) = n\langle P(\vec{Q})S(\vec{Q})\rangle \qquad (3)$$

where n is a prefactor related to the number density of silica powder in the neutron beam. $P(\vec{Q})$ (high Q region) represents CO_2 loaded mesopores. $S(\vec{Q})$ (low Q region) provides information on the hexagonally packed cylindrical pores in MCM-41 and SBA-15 matrices.

$S(\vec{Q})$ modeling at $Q < 0.04$ Å^{-1} suggests that the scattering intensity follows a power law trend ($I(Q) \sim Q^{-D}$) with slopes of 3.64 ± 0.13 and 3.80 ± 0.20 in MCM-41 and SBA-15, respectively (see Fig. 2). The power law slopes of $3 < D < 4$ indicates scattering from surface geometry or pore size polydispersity.[76,77] As $S(\vec{Q})$ retains a relatively unchanged power law slope values, it can be inferred that increasing CO_2 pressure has a negligible impact on the morphology of MCM-41 and SBA-15 matrices. These observations are consistent with that of confined methane in porous silica with similar pore sizes.[51]

The pressure effect on the form factor, $P(\vec{Q})$ is more significant compared to that on $S(\vec{Q})$ and was monitored by observing the change in the first-order peak behavior. Under vacuum, the first-order peak intensity of MCM-41 and SBA-15 powders are located at Q of about 0.17 Å^{-1} and 0.074 Å^{-1},

respectively (see Fig. 2). The peak positions suggest that the mesopores in the silica matrices are aligned in a *p6mm* hexagonal packing[78] with pore-center to pore-center distances of 42.93 Å and 99.11 Å in MCM-41 and SBA-15 matrices, respectively. These results are in agreement with previous studies that discussed methane organization in architected porous silica materials.[51,79,80] As the pressure increases, the intensity of the first order peaks decreases considerably in both MCM-41 and SBA-15 mesopores to reach its minimum at the highest applied pressures (55 bars). Slight decrease in the peak intensity is observed in MCM-41 as the pressure increase from vacuum to 24.88 bar followed by a significant drop on increasing the pressure to 44.89 bars (see Fig. 3(a)). However, in SBA-15, slight decrease was noticed as the pressure increase to 34.91 followed by a substantial decrease as the pressure increased to 55.52 bar (see Fig. 3(b)). This decline is mainly attributed to the reduction of the scattering contrast between the pore surface and the adsorbed CO_2 molecules on that surface. A quantitative analysis of the peak intensities as a function of the pressure is obtained by calculating the full width half maximum (FWHM) using Gaussian fitting (see Fig. 3(c) and (d)) as follows, where C is the scale factor and σ is the peak width (FWHM/2.345).[81]
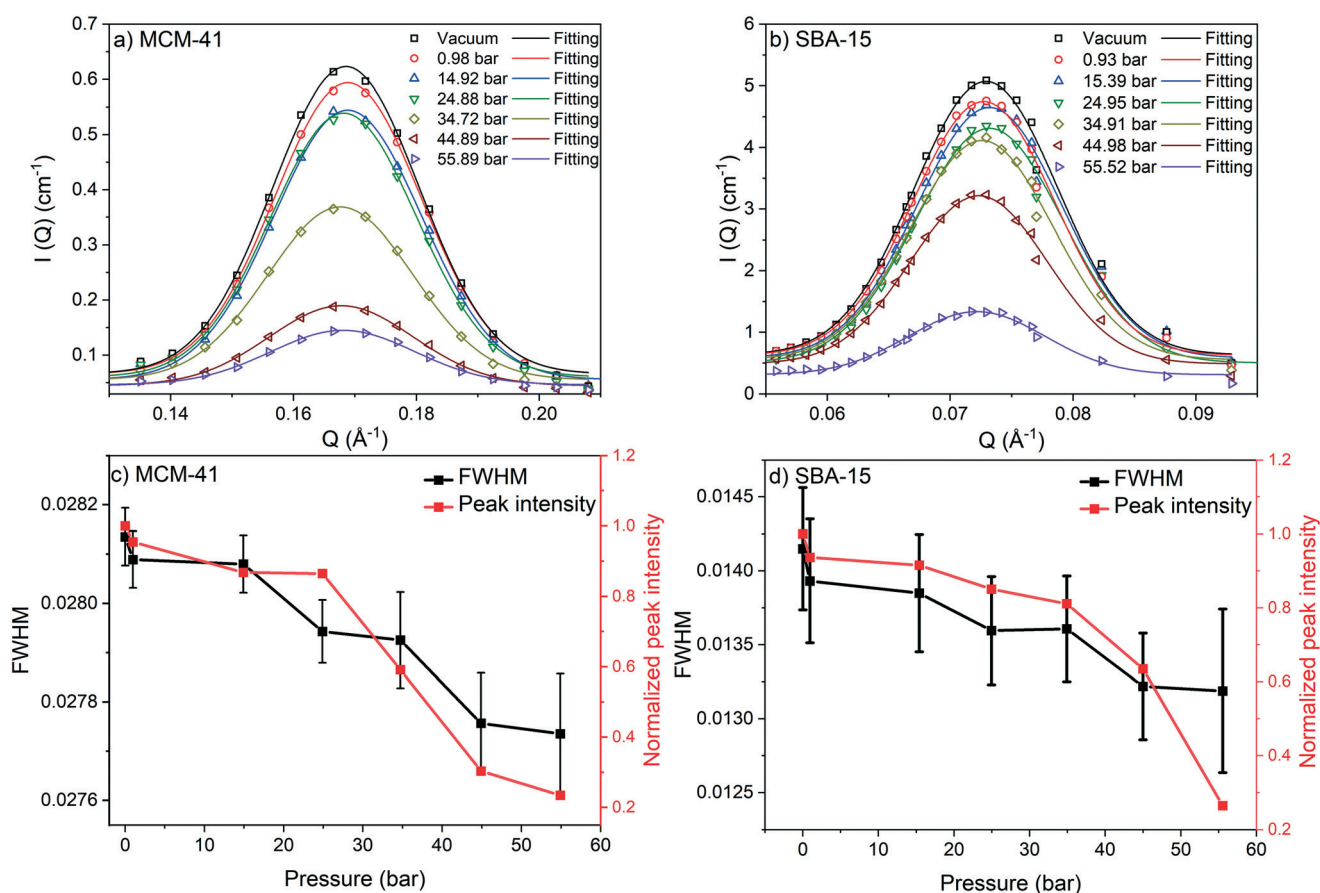

Fig. 3 The fitted first-order peak intensity of MCM–41 and SBA-15 as a function of the applied pressure are represented in (a) and (b), respectively. The full width half maximum (FWHM) and the peak intensity normalized by the intensity of the pore under vacuum for MCM–41 and SBA-15 are shown in (c) and (d), respectively.

$$I(Q) = C \exp\left[-\frac{(Q - Q_o)^2}{2\sigma^2}\right] + \text{Background} \qquad (4)$$

FWHM for MCM-41 and SBA-15 showed a systematic decrease with an increase in the pressure (Fig. 3(c) and (d)). The observed profiles of FWHM are resulted from the magnitude of the peak intensity decrease as the pressure increase. Similarly, the normalized peak intensity decreased substantially from 1 to about 0.2 as the pressure increase from 0 to 55 bar, respectively.

As CO_2 molecules are adsorbed on the pore surfaces of MCM-41 and SBA-15, the contrast between the pore surface and the adsorbed gas layer decreases. The scattering length density (SLD) of amorphous silica is 3.21×10^{-6} Å^{-2} at a mass density of 2.20 g cm^{-3}.[82] SLD of the adsorbed CO_2, in Å^{-2} units, is proportional to the density of the adsorbed layer on the pore surface such that:

$$\rho_{\text{SLD}} = (2.49 \times \rho_{CO_2}) \times 10^{-6} \qquad (5)$$

where ρ is the mass density of the adsorbed gas.[63] The maximum scattering contrast is under vacuum due to the difference between the SLD of the amorphous silica matrices and that of the vacuum inside the pore, which is 0. This contrast decreases as CO_2 molecules adsorb on the pore
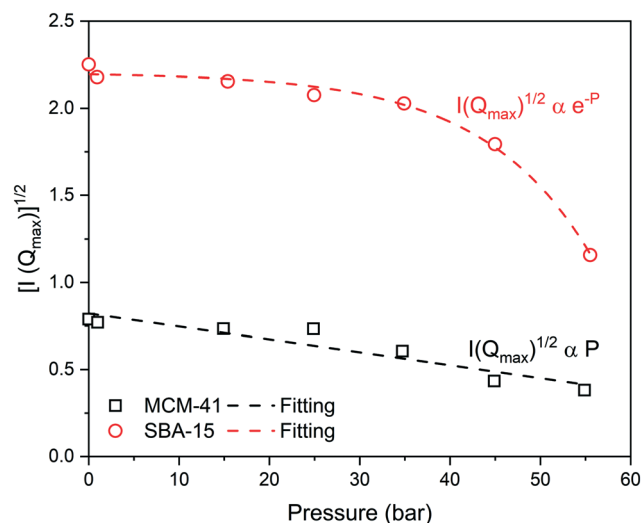

Fig. 4 The amplitudes of the SANS intensity $[I(Q_{max})^{1/2}]$ at the maximum of the first-order peak as a function of the applied pressure in MCM-41 and SBA-15 pores are shown. The pressures at which the intensity reaches zero average contrast in MCM-41 and SBA-15 are about 110 bar and 72 bar, respectively.

surface and develop a finite SLD that reduces the density difference ($\Delta\rho$) with the silica matrix. The density of the adsorbed CO_2 increases as the pressure increase which
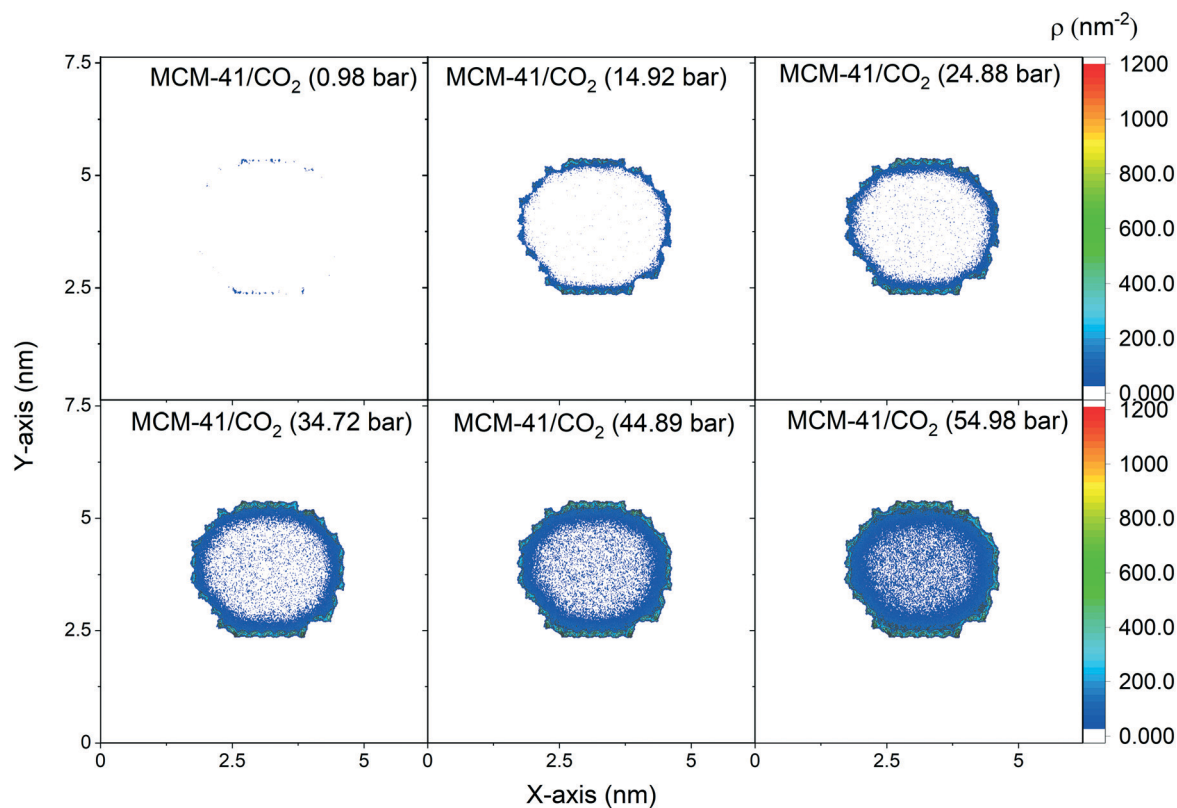

Fig. 5 The 2D density maps of the CO_2 molecules adsorbed on the pore walls of MCM-41 as a function of the pressure obtained from the classical molecular dynamics simulations are shown. The pore diameter of MCM-41 is 3.3 nm. The density maps are averaged over the last 10 ns of the simulation time.

This journal is © The Royal Society of Chemistry 2021

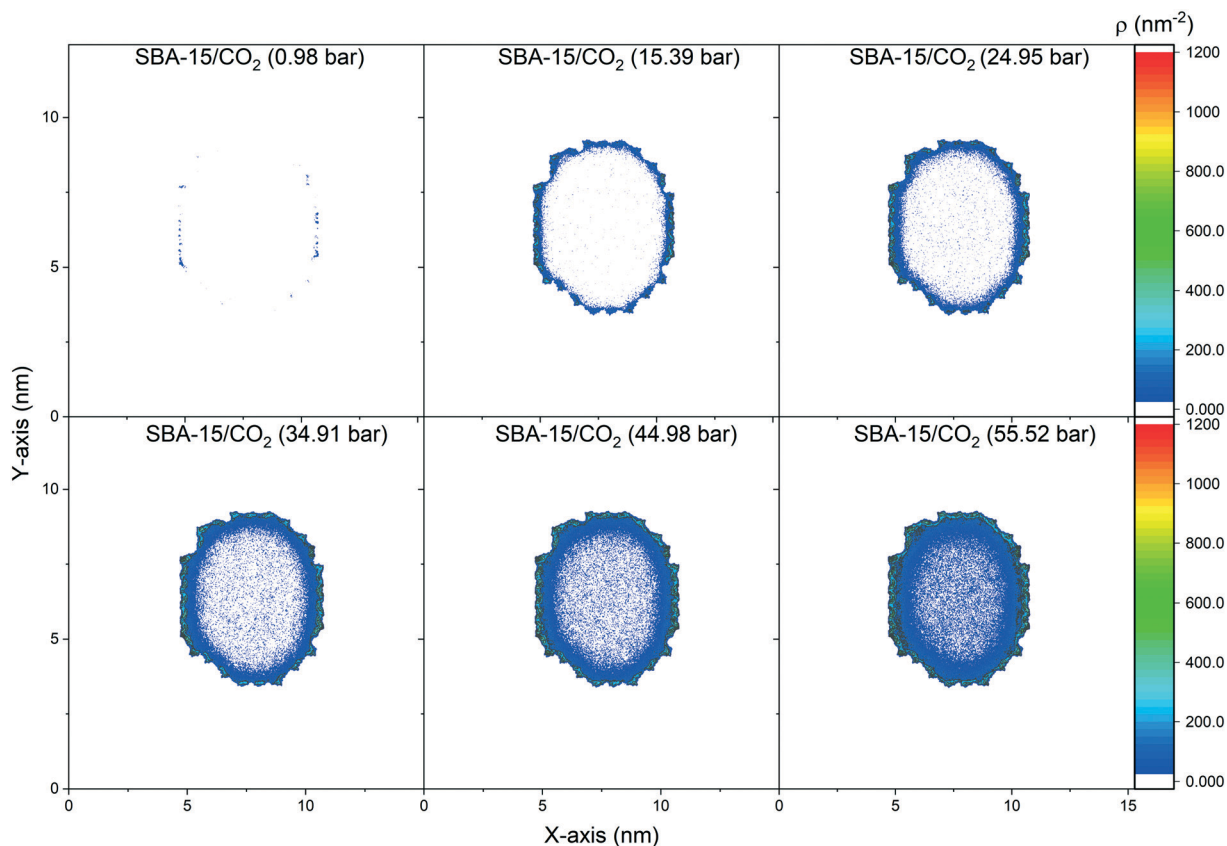*Environ. Sci.: Nano*, 2021, **8**, 2006–2018 | **2011**

Fig. 6 The 2D density maps of the CO_2 molecules adsorbed on the pore walls of SBA-15 as a function of the pressure obtained from the classical molecular dynamics simulations are shown. The pore diameter of SBA-15 is 6.8 nm. The density maps are averaged over the last 10 ns of the simulation time.

contributes to a significant decrease in the scattering contrast. These observations are consistent with previous studies after accounting for the differences in the adsorbate chemistry.[82,83] It is interesting to note that the decrease in the amplitude of scattering intensity of MCM-41 and SBA-15 is more significant when CO_2 adsorbs on their pore surface compared to CD_4.[51]

The neutron scattering intensity of binary systems, such as CO_2–silica system, is proportional to the difference of the SLD of the scattering object and the surrounding medium.[63] Thus, the contrast matching point, the point at which the contrast between the silica matrix and the adsorbed CO_2 becomes zero (*i.e.*, $I(Q) = 0$).[83,84] can be estimated by plotting the square root of the maximum intensity $[I(Q_{max})^{1/2}]$ as a function of the applied pressure (see Fig. 4). It is interesting to observe that $I(Q_{max})^{1/2}$ decreases linearly with pressure in MCM-41 while exponential decay is noted in SBA-15 pores. The pressure at which the contrast matching point occurs in MCM-41 is about 110 bar, which corresponds to a density of 0.83 g cm^{-3}. In SBA-15, the contrast matching point occurs at a pressure of about 72 bar which corresponds to 0.75 g cm^{-3}. The lower pressure required to reach the contrast matching point in SBA-15 can be attributed to the larger pore size that results in higher CO_2 partitioning into the pore space compared to MCM-41.

The spatial distribution of the adsorbed CO_2 molecules on the pore surfaces is determined by calculating the 2D density maps over the axis parallel to the pore length (*z*-axis) using MD simulations (Fig. 5 and 6). Anisotropic distribution of confined CO_2 is observed in both MCM-41 and SBA-15 pore spaces, with higher densities noted at the pore surfaces compared to the center of the pore which is attributed to confinement effect.[35,85–87] At pressures under 15 bars, almost all the confined molecules were adsorbed on the MCM-41 and SBA-15 pore surfaces. Traces of CO_2 molecules are distributed unevenly outside the adsorbed layers and closer to the pore center. The thickness of the adsorbed layer and the concentrations of CO_2 molecules closer to the center of the pore were systematically increased as the pressure increased from about 1 bar to about 55 bar. The anisotropic distribution of CO_2 molecules in MCM-41 and SBA-15 pores are also evident from the snapshots taken from the equilibrated trajectories during the last 1 ns of the simulation time (see Fig. S2†).

3.2. Core–shell structure of confined CO_2

The experimental SANS intensities of the confined CO_2 in MCM-41 and SBA-15 are modeled using a core–shell cylindrical geometry with multilevel densities to probe the

Fig. 7 The thickness of the adsorbed CO_2 layer determined from the small-angle neutron scattering measurements and molecular dynamics simulations (a) and the corresponding core radius (b) as a function of the applied pressure are shown. The error bars of the SANS and MD data represent standard deviations based on fittings and simulations performed in triplicates.

Fig. 8 The radial distribution functions and the corresponding coordination numbers of –OH–C_{CO_2} in the MCM-41 (a) and SBA-15 (b) as a function of the applied pressure are shown. The simulation data are averaged over the last 10 ns of the simulation time.

pressure dependent shell thickness and core radius.[79,80,88,89] The shell is defined as the thickness of the adsorbed CO_2 layer on the pore surface while the core is the diameter of the silica pore excluding the CO_2 shell. These data are then compared with the MD simulation data to determine the density of the confined fluids (see Fig. 7 and Table S2†). The shell thickness are obtained from SANS measurements by utilizing the model developed by Chiang and co-workers,[79,80] while those from MD simulations are directly calculated from the 2D density maps. The model developed by Chiang and co-workers involves the shell thickness of the adsorbed gas, the core radius and the scattering length densities of the adsorbed gas and silica matrix (see Fig. S3†). This model has been applied to predict the adsorption extent of CD_4 in MCM-41 and SBA-15 with cylindrical pore geometries. The shell boundaries in MD density maps are the pore surface and the point where the density of the adsorbed CO_2 start to decline steeply.[51]

The shell thickness of the adsorbed CO_2 molecules on MCM-41 and SBA-15 pore surfaces increased systematically with the pressure as indicated by SANS measurements and MD simulations (see Fig. 7). The experimentally determined shell thicknesses of adsorbed CO_2 on MCM-41 using SANS measurements are 0.7 ± 0.1 Å, 2.1 ± 0.1 Å, 2.2 ± 0.1 Å, 6.7 ± 0.1 Å, 11.5 ± 0.2 Å, and 12.6 ± 0.1 Å at pressures of about 1.0, 14.9, 24.9, 34.7, 45.0 and 54.9 bar, respectively. The thickness
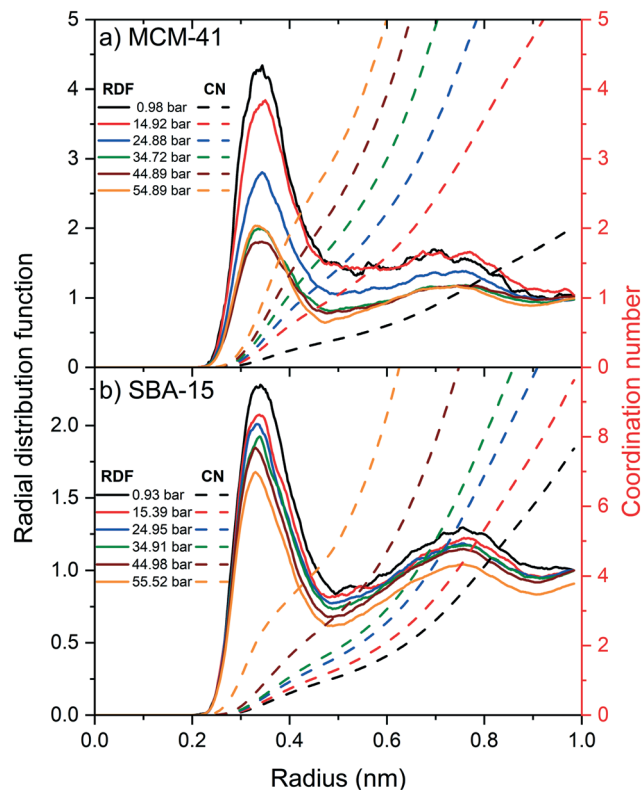
of the adsorbed CO_2 layer on SBA-15 pore surfaces are 1.9 ± 0.1, 2.6 ± 0.1, 4.9 ± 0.1, 8.3 ± 0.1, 12.4 ± 0.1, and 20.0 ± 0.1 at pressures of about 0.9, 15.4, 24.9, 34.9, 45.0 and 55.5 bar, respectively. The thickness of the adsorbed CO_2 molecules, also referred to as "shell" determined experimentally are in close agreement with that of classical MD simulations (see Fig. 7(a)).

The increase in the shell thickness of the adsorbed CO_2 on MCM-41 and SBA-15 surfaces are more significant than that of CD_4 adsorption even at higher pressures.[51] The increase in the shell thickness is associated with a considerable decrease in the core radius in MCM-41 and SBA-15 pores (see Fig. 7(b)). The core radius in MCM-41 decreased from 16.1 ± 0.2 Å to 4.9 ± 0.1 Å as the pressure increases from 1.0 to 55 bar, respectively, while the core radius in SBA-15 decreased from 31.7 ± 0.3 Å to 9.9 ± 0.1 Å, respectively.

The radial distribution function (RDF) and the associated coordination number (CN) of carbon atom in CO_2 molecules from the hydroxyl group (–OH) on the pore surface are calculated to probe the influence of the applied pressure on the organization and the structure of the adsorbed CO_2 layers on MCM-41 and SBA-15 pore surfaces (see Fig. 8). The RDF peaks in MCM-41 and SBA-15 decreased systematically with an increase in the pressure, suggesting more substantial increase in CO_2 density beyond the adsorbed layer. Further, RDF peaks in MCM-41 is higher than that in SBA-15 at the

This journal is © The Royal Society of Chemistry 2021

Environ. Sci.: Nano, 2021, **8**, 2006–2018 | **2013**

Fig. 9 The number of carbon atoms in the first coordination shells of the –OH group on the MCM-41 and SBA-15 pore surfaces obtained from the RDFs are shown. The error bars represent the standard deviations from simulations performed in triplicates.

same pressure which can be attributed to the higher confinement effect in the narrower pores.

Although RDF peaks intensities decrease with an increase in pressure, the corresponding CN profiles showed a substantial increase in both MCM-41 and SBA-15 which imply an increase in the density of carbon atoms in the first coordination shell of –OH group and the adjacent interfacial layers. The number of carbon atoms in the first coordination shell corresponding to the pressure is calculated by integrating the coordination number at the end of the RDF peak and depicted in Fig. 9. The number of carbon atoms in the first coordination shell of –OH on MCM-41 increased from 0.5 ± 0.1 to 2.8 ± 0.1 as the pressure increased from 1.0 bar to 54.9 bar, respectively. Sharper increase in the number of C atoms in the first coordination shell of OH is noticed on MCM-41 pores as the pressure increase from about 0.98 to 14.92 bars compared to the change in higher pressures. This trend is attributed to the relatively higher pressure increment (~14 bar) compared to the following pressure change values (~10 bar). In SBA-15, the number of carbon atoms increased from 0.3 ± 0.1 to 1.3 ± 0.1 as the pressure increased from 0.9 bar to 55.5 bar, respectively. The number of CO_2 carbon atoms in the first coordination shell of OH groups on MCM-41 and SBA-15 are significantly higher than that of CH_4 carbon atoms due to the higher tendency to adsorb CO_2 on silica surfaces, which is in agreement with previous studies.[86,90,91]

3.3. Energetics of CO_2 adsorption in MCM-41 and SBA-15

Further insights on the adsorption and organization of adsorbed CO_2 molecules on MCM-41 and SBA-15 pore surfaces are obtained by calculating the intermolecular interactions. Here, the energetics of CO_2 adsorption are

Fig. 10 The electrostatic and van der Waals interaction energy associated with the adsorption of CO_2 molecules on the surfaces of MCM-41 and SBA-15 materials as a function of pressure are shown. These analyses are performed on data averaged over the last 10 ns of the simulation time. The error bars are calculated based on the simulations performed in triplicates.

obtained by calculating the magnitude of van der Waals and electrostatic potentials as a function of the applied pressure (see Fig. 10). van der Waals and electrostatic interactions are normalized by the number of –OH group in the MCM-41 and SBA-15 pore surface, which are 128 and 256, respectively, for a consistent comparison. Both van der Waals and electrostatic interactions are significantly enhanced with increase in pressure, which corresponds to higher extents of CO_2 adsorption. In this context, the van der Waals interactions in MCM-41 are enhanced from -0.8 ± 0.1 to -5.8 ± 0.1 kJ mol^{-1} as the pressure increases from 1.0 to 54.9 bar. Similarly, as the pressure increased from 0.9 to 55.9 bar in SBA 15, the favorable van der Waals interactions are enhanced from -1.2 ± 0.1 to -5.8 ± 0.1 kJ mol^{-1}. Similarly, the electrostatic interactions in MCM-41 are enhanced from -0.13 ± 0.01 to -1.3 ± 0.1 kJ mol^{-1} as the pressure increases from 1.0 to 54.9 bar. In SBA-15, the electrostatic interactions are enhanced from -0.4 ± 0.03 to -2.8 ± 0.05 kJ mol^{-1} as the pressure increased from 0.9 to 56.0 bar, respectively.

The intermolecular interactions suggest that CO_2 adsorption on silica surfaces is primarily driven by Lennard-

Jones interactions, arising from the atomistic collisions, with smaller contributions from the electrostatic interactions. It is interesting to note that the electrostatic contributions are more significant in the case of CO_2 molecules confined in silica nanopores compared to CH_4 molecules in confinement.[51] In additions to the contributions of van der Waals and electrostatic interactions on CO_2 adsorption behavior in MCM-41 and SBA-15 pores, CO_2 molecules form hydrogen bonds with the OH groups on the pore surface that contribute positively to the overall intermolecular interactions. The energy of the individual hydrogen bond can vary from 1 to 40 kcal mol^{-1}.[92] The number of hydrogen bonds in SBA-15 is higher than that in MCM-41 due to the higher number of OH groups on the pore surface and the higher number of CO_2 molecules in confinement. The total number of hydrogen bonds between OH group on the pore surface and the confined CO_2 increase with the pressure in both MCM-41 and SBA-15 pores (see Table S3†) due to the higher adsorption extent of CO_2 molecules on the pore surface. Further, the intermolecular interactions between CO_2 molecules confined in MCM-41 and SBA-15 are dominated by van der Waals attractions with a considerable contribution from electrostatic attractions (see Table S4†). The combination of van der Waals, electrostatic and hydrogen bonds contribute to higher energies of adsorption of CO_2 on MCM-41 and SBA-15 surfaces compared to CH_4.[51]

4. Conclusions

The structure of confined CO_2 in mesoporous silica, MCM-41 with pore diameter of 3.3 nm and SBA-15 with 6.8 nm, was studied as a function of pressures applied that range from vacuum to about 55 bars using *in situ* small angle neutron scattering and classical molecular dynamics simulations. SANS measurements showed that higher levels of CO_2 are adsorbed with increasing pressure of CO_2. Core–shell organization of the CO_2 molecules in confinement are noted with the adsorbed CO_2 molecules forming a shell-like structure and less dense CO_2 molecules in the center of the pore. The shell thickness increases systematically with pressure, while the corresponding core radius decreases accordingly. The core–shell structures of CO_2 predicted from MD simulations are in close agreement with the experimental SANS data. Our calculations using MD simulations show that CO_2 adsorption is primarily driven by van der Waals interactions with electrostatic interactions having a smaller contribution. These studies demonstrate that the structure of confined CO_2 molecules can be experimentally determined, and these experimental results can be used to validate modeling efforts. The experimental and modeling approaches discussed in this study can be used to determine the organization of confined CO_2 molecules in novel functionalized materials and in natural geologic minerals.

Conflicts of interest

There are no conflicts to declare.

Acknowledgements

References

1 D. Chakraborty and P. K. Chattaraj, Bonding, reactivity, and dynamics in confined systems, *J. Phys. Chem. A*, 2019, **123**(21), 4513–4531.

2 S. Fleischmann, M. A. Spencer and V. Augustyn, Electrochemical Reactivity under Confinement Enabled by Molecularly Pillared 2D and Layered Materials, *Chem. Mater.*, 2020, **32**(8), 3325–3334.

3 P. Kondratyuk and J. T. Yates, Effects of Molecular Confinement inside Single Walled Carbon Nanotubes on Chemical Reactivity– Atomic H+ 1-Heptene, *J. Am. Chem. Soc.*, 2007, **129**(28), 8736–8739.

4 A. L. Harrison, G. M. Dipple, I. M. Power and K. U. Mayer, Influence of surface passivation and water content on mineral reactions in unsaturated porous media: Implications for brucite carbonation and CO2 sequestration, *Geochim. Cosmochim. Acta*, 2015, **148**, 477–495.

5 P. Sun, J. R. Grace, C. J. Lim and E. J. Anthony, A discrete-pore-size-distribution-based gas–solid model and its application to the CaO + CO_2 reaction, *Chem. Eng. Sci.*, 2008, **63**(1), 57–70.

6 M. Chen, N. Wang, J. Yu and A. Yamaguchi, Effect of porosity on carbonation and hydration resistance of CaO materials, *J. Eur. Ceram. Soc.*, 2007, **27**(4), 1953–1959.

7 M. Liu and G. Gadikota, Integrated CO_2 capture, conversion, and storage to produce calcium carbonate using an amine looping strategy, *Energy Fuels*, 2018, **33**(3), 1722–1733.

8 M. Liu, H. Asgar, S. Seifert and G. Gadikota, Novel aqueous amine looping approach for the direct capture, conversion and storage of CO_2 to produce magnesium carbonate, *Sustainable Energy Fuels*, 2020, **4**(3), 1265–1275.

9 M. Liu and G. Gadikota, Single-step, low temperature and integrated CO_2 capture and conversion using sodium glycinate to produce calcium carbonate, *Fuel*, 2020, **275**, 117887.

10 G. Gadikota, Multiphase carbon mineralization for the reactive separation of CO_2 and directed synthesis of H_2, *Nat. Rev. Chem.*, 2020, **4**(2), 78–89.

11 G. Gadikota, J. Matter, P. Kelemen and A. H. A. Park, Chemical and morphological changes during olivine carbonation for CO_2 storage in the presence of NaCl and NaHCO$_3$, *Phys. Chem. Chem. Phys.*, 2014, **16**(10), 4679–4693.

This journal is © The Royal Society of Chemistry 2021

Environ. Sci.: Nano, 2021, **8**, 2006–2018 | **2015**

12 G. Gadikota, J. Matter, P. Kelemen, P. V. Brady and A. H. A. Park, Elucidating the differences in the carbon mineralization behaviors of calcium and magnesium bearing alumino-silicates and magnesium silicates for CO_2 storage, *Fuel*, 2020, **277**, 117900.

13 A. Brunetti, F. Scura, G. Barbieri and E. Drioli, Membrane technologies for CO_2 separation, *J. Membr. Sci.*, 2010, **359**(1–2), 115–125.

14 D. Aaron and C. Tsouris, Separation of CO_2 from flue gas: a review, *Sep. Sci. Technol.*, 2005, **40**(1–3), 321–348.

15 E. J. Garcia, J. Pérez-Pellitero, G. D. Pirngruber, C. Jallut, M. Palomino, F. Rey and S. Valencia, Tuning the adsorption properties of zeolites as adsorbents for CO_2 separation: best compromise between the working capacity and selectivity, *Ind. Eng. Chem. Res.*, 2014, **53**(23), 9860–9874.

16 R. V. Siriwardane, M. S. Shen, E. P. Fisher and J. A. Poston, Adsorption of CO_2 on molecular sieves and activated carbon, *Energy Fuels*, 2001, **15**(2), 279–284.

17 N. P. Wickramaratne and M. Jaroniec, Activated carbon spheres for CO_2 adsorption, *ACS Appl. Mater. Interfaces*, 2013, **5**(5), 1849–1855.

18 M. Cinke, J. Li, C. W. Bauschlicher Jr, A. Ricca and M. Meyyappan, CO_2 adsorption in single-walled carbon nanotubes, *Chem. Phys. Lett.*, 2003, **376**(5–6), 761–766.

19 R. V. Siriwardane, M. S. Shen, E. P. Fisher and J. Losch, Adsorption of CO_2 on zeolites at moderate temperatures, *Energy Fuels*, 2005, **19**(3), 1153–1159.

20 M. R. Hudson, W. L. Queen, J. A. Mason, D. W. Fickel, R. F. Lobo and C. M. Brown, Unconventional, highly selective CO_2 adsorption in zeolite SSZ-13, *J. Am. Chem. Soc.*, 2012, **134**(4), 1970–1973.

21 D. Saha, Z. Bao, F. Jia and S. Deng, Adsorption of CO_2, CH_4, N_2O, and N_2 on MOF-5, MOF-177, and zeolite 5A, *Environ. Sci. Technol.*, 2010, **44**(5), 1820–1826.

22 C. Chen and W. S. Ahn, CO_2 capture using mesoporous alumina prepared by a sol–gel process, *Chem. Eng. J.*, 2011, **166**(2), 646–651.

23 C. Chen, S. Zhang, K. H. Row and W. S. Ahn, Amine–silica composites for CO_2 capture: A short review, *J. Energy Chem.*, 2017, **26**(5), 868–880.

24 R. Ullah, M. Atilhan, S. Aparicio, A. Canlier and C. T. Yavuz, Insights of CO_2 adsorption performance of amine impregnated mesoporous silica (SBA-15) at wide range pressure and temperature conditions, *Int. J. Greenhouse Gas Control*, 2015, **43**, 22–32.

25 G. Jiang, Q. Huang, S. D. Kenarsari, X. Hu, A. G. Russell, M. Fan and X. Shen, A new mesoporous amine-TiO2 based pre-combustion CO_2 capture technology, *Appl. Energy*, 2015, **147**, 214–223.

26 Y. Kong, X. Shen, S. Cui and M. Fan, Development of monolithic adsorbent via polymeric sol–gel process for low-concentration CO_2 capture, *Appl. Energy*, 2015, **147**, 308–317.

27 J. Yu, L. H. Xie, J. R. Li, Y. Ma, J. M. Seminario and P. B. Balbuena, CO_2 capture and separations using MOFs: computational and experimental studies, *Chem. Rev.*, 2017, **117**(14), 9674–9754.

28 A. Torrisi, R. G. Bell and C. Mellot-Draznieks, Functionalized MOFs for enhanced CO_2 capture, *Cryst. Growth Des.*, 2010, **10**(7), 2839–2841.

29 J. Liu, Y. Wei and Y. Zhao, Trace carbon dioxide capture by metal–organic frameworks, *ACS Sustainable Chem. Eng.*, 2018, **7**(1), 82–93.

30 M. Niu, H. Yang, X. Zhang, Y. Wang and A. Tang, Amine-impregnated mesoporous silica nanotube as an emerging nanocomposite for CO_2 capture, *ACS Appl. Mater. Interfaces*, 2016, **8**(27), 17312–17320.

31 X. Xu, C. Song, J. M. Andresen, B. G. Miller and A. W. Scaroni, Preparation and characterization of novel CO_2 "molecular basket" adsorbents based on polymer-modified mesoporous molecular sieve MCM-41, *Microporous Mesoporous Mater.*, 2003, **62**(1–2), 29–45.

32 K. L. Stefanopoulos, T. A. Steriotis, F. K. Katsaros, N. K. Kanellopoulos, A. C. Hannon and J. D. F. Ramsay, Structural study of supercritical carbon dioxide confined in nanoporous silica by in situ neutron diffraction, *J. Phys.: Conf. Ser.*, 2012, **340**(1), 012049.

33 A. Danon, P. C. Stair and E. Weitz, FTIR study of CO_2 adsorption on amine-grafted SBA-15: elucidation of adsorbed species, *J. Phys. Chem. C*, 2011, **115**(23), 11540–11549.

34 G. Rother, L. Vlcek, M. S. Gruszkiewicz, A. A. Chialvo, L. M. Anovitz, J. L. Banuelos, D. Wallacher, N. Grimm and D. R. Cole, Sorption phase of supercritical CO_2 in silica aerogel: experiments and mesoscale computer simulations, *J. Phys. Chem. C*, 2014, **118**(28), 15525–15533.

35 S. Mohammed and G. Gadikota, CO_2-Induced displacement and diffusive transport of shale geofluids in silica nanopores of varying sizes, *J. CO2 Util.*, 2019, **32**, 37–45.

36 S. Mohammed and G. Gadikota, Exploring the Role of Inorganic and Organic Interfaces on CO_2 and CH_4 Partitioning: Case Study of Silica, Illite, Calcite, and Kerogen Nanopores on Gas Adsorption and Nanoscale Transport Behaviors, *Energy Fuels*, 2020, **34**(3), 3578–3590.

37 T. Le, A. Striolo and D. R. Cole, CO_2–C_4H_{10} mixtures simulated in silica slit pores: relation between structure and dynamics, *J. Phys. Chem. C*, 2015, **119**(27), 15274–15284.

38 J. Liu, Y. Wei, P. Li, Y. Zhao and R. Zou, Selective H_2S/CO_2 separation by metal–organic frameworks based on chemical-physical adsorption, *J. Phys. Chem. C*, 2017, **121**(24), 13249–13255.

39 H. Seema, K. C. Kemp, N. H. Le, S. W. Park, V. Chandra, J. W. Lee and K. S. Kim, Highly selective CO_2 capture by S-doped microporous carbon materials, *Carbon*, 2014, **66**, 320–326.

40 H. S. Choi and M. P. Suh, Highly selective CO_2 capture in flexible 3D coordination polymer networks, *Angew. Chem., Int. Ed.*, 2009, **48**(37), 6865–6869.

41 A. L. Chaffee, G. P. Knowles, Z. Liang, J. Zhang, P. Xiao and P. A. Webley, CO_2 capture by adsorption: materials and process development, *Int. J. Greenhouse Gas Control*, 2007, **1**(1), 11–18.

42 S. Mohammed and G. Gadikota, The effect of hydration on the structure and transport properties of confined carbon

2016 | *Environ. Sci.: Nano*, 2021, **8**, 2006–2018

This journal is © The Royal Society of Chemistry 2021

dioxide and methane in calcite nanopores, *Front. Energy Res.*, 2018, **6**, 86.

43 S. B. Badmos, T. Bui, A. Striolo and D. R. Cole, Factors Governing the Enhancement of Hydrocarbon Recovery via H_2S and/or CO_2 Injection: Insights from a Molecular Dynamics Study in Dry Nanopores, *J. Phys. Chem. C*, 2019, **123**(39), 23907–23918.

44 T. T. B. Le, A. Striolo and D. R. Cole, Partial CO_2 Reduction in Amorphous Cylindrical Silica Nanopores Studied with Reactive Molecular Dynamics Simulations, *J. Phys. Chem. C*, 2019, **123**(43), 26358–26369.

45 S. B. Badmos, N. Islam, U. Shah, A. Striolo and D. R. Cole, Competitive adsorption and reduced mobility: N-octane, CO_2 and H_2S in alumina and graphite pores, *Mol. Phys.*, 2020, 1–12.

46 S. B. Badmos, A. Striolo and D. R. Cole, Aqueous hydrogen sulfide in slit-shaped silica nanopores: confinement effects on solubility, structural, and dynamical properties, *J. Phys. Chem. C*, 2018, **122**(26), 14744–14755.

47 M. Lasich, Adsorption of H_2S from Hydrocarbon Gas Using Doped Bentonite: A Molecular Simulation Study, *ACS Omega*, 2020, **5**(31), 19877–19883.

48 S. Cai, Q. Li, C. Liu and X. Liu, The adsorption of hydrogen sulfide in calcite pores: A molecular simulation study, *J. Mol. Liq.*, 2020, **299**, 112253.

49 M. S. Santos, L. F. Franco, M. Castier and I. G. Economou, Molecular dynamics simulation of n-alkanes and CO_2 confined by calcite nanopores, *Energy Fuels*, 2018, **32**(2), 1934–1941.

50 M. Makaremi, K. D. Jordan, G. D. Guthrie and E. M. Myshakin, Multiphase Monte Carlo and molecular dynamics simulations of water and CO_2 intercalation in montmorillonite and beidellite, *J. Phys. Chem. C*, 2015, **119**(27), 15112–15124.

51 S. Mohammed, M. Liu, Y. Liu and G. Gadikota, Probing the Core-Shell Organization of Nano-Confined Methane in Cylindrical Silica Pores Using In-Situ Small-Angle Neutron Scattering and Molecular Dynamics Simulations, *Energy Fuels*, 2020, **34**(12), 15246–15256.

52 T. A. Makal, J. R. Li, W. Lu and H. C. Zhou, Methane storage in advanced porous materials, *Chem. Soc. Rev.*, 2012, **41**(23), 7761–7779.

53 Y. He, W. Zhou, G. Qian and B. Chen, Methane storage in metal–organic frameworks, *Chem. Soc. Rev.*, 2014, **43**(16), 5657–5678.

54 V. Rozyyev, D. Thirion, R. Ullah, J. Lee, M. Jung, H. Oh, M. Atilhan and C. T. Yavuz, High-capacity methane storage in flexible alkane-linked porous aromatic network polymers, *Nat. Energy*, 2019, **4**(7), 604–611.

55 K. M. Thomas, Hydrogen adsorption and storage on porous materials, *Catal. Today*, 2007, **120**(3–4), 389–398.

56 Q. Weng, X. Wang, C. Zhi, Y. Bando and D. Golberg, Boron nitride porous microbelts for hydrogen storage, *ACS Nano*, 2013, **7**(2), 1558–1565.

57 S. J. Yang, T. Kim, J. H. Im, Y. S. Kim, K. Lee, H. Jung and C. R. Park, MOF-derived hierarchically porous carbon with exceptional porosity and hydrogen storage capacity, *Chem. Mater.*, 2012, **24**(3), 464–470.

58 R. E. Morris and P. S. Wheatley, Gas storage in nanoporous materials, *Angew. Chem., Int. Ed.*, 2008, **47**(27), 4966–4981.

59 S. Ma and H. C. Zhou, Gas storage in porous metal–organic frameworks for clean energy applications, *Chem. Commun.*, 2010, **46**(1), 44–53.

60 Y. B. Melnichenko, H. Mayama, G. Cheng and T. Blach, Monitoring phase behavior of sub-and supercritical CO_2 confined in porous fractal silica with 85% porosity, *Langmuir*, 2010, **26**(9), 6374–6379.

61 S. Ciccariello, Y. B. Melnichenko and L. He, Phase behavior of carbon dioxide confined in silica aerogel in the vicinity of the bulk critical point, *J. Phys. Chem. C*, 2011, **115**(45), 22336–22346.

62 A. Holewinski, M. A. Sakwa-Novak and C. W. Jones, Linking CO_2 sorption performance to polymer morphology in aminopolymer/silica composites through neutron scattering, *J. Am. Chem. Soc.*, 2015, **137**(36), 11749–11759.

63 Y. B. Melnichenko, *Small-Angle Scattering from Confined and Interfacial Fluids*, Springer, 2016.

64 S. R. Kline, Reduction and analysis of SANS and USANS data using IGOR Pro, *J. Appl. Crystallogr.*, 2006, **39**(6), 895–900.

65 J. P. Perdew, K. Burke and M. Ernzerhof, Generalized gradient approximation made simple, *Phys. Rev. Lett.*, 1996, **77**(18), 3865.

66 J. D. Head and M. C. Zerner, A Broyden—Fletcher—Goldfarb—Shanno optimization procedure for molecular geometries, *Chem. Phys. Lett.*, 1985, **122**(3), 264–270.

67 A. Phan, D. R. Cole and A. Striolo, Aqueous methane in slit-shaped silica nanopores: high solubility and traces of hydrates, *J. Phys. Chem. C*, 2014, **118**(9), 4860–4868.

68 T. Bui, A. Phan, D. R. Cole and A. Striolo, Transport mechanism of guest methane in water-filled nanopores, *J. Phys. Chem. C*, 2017, **121**(29), 15675–15686.

69 R. T. Cygan, J. J. Liang and A. G. Kalinichev, Molecular models of hydroxide, oxyhydroxide, and clay phases and the development of a general force field, *J. Phys. Chem. B*, 2004, **108**(4), 1255–1266.

70 J. J. Potoff and J. I. Siepmann, Vapor–liquid equilibria of mixtures containing alkanes, carbon dioxide, and nitrogen, *AIChE J.*, 2001, **47**(7), 1676–1682.

71 S. Nosé, A molecular dynamics method for simulations in the canonical ensemble, *Mol. Phys.*, 1984, **52**(2), 255–268.

72 W. G. Hoover, Canonical dynamics: equilibrium phase-space distributions, *Phys. Rev. A: At., Mol., Opt. Phys.*, 1985, **31**(3), 1695.

73 T. Darden, D. York and L. Pedersen, Particle mesh Ewald: An N·log(N) method for Ewald sums in large systems, *J. Chem. Phys.*, 1993, **98**(12), 10089–10092.

74 M. J. Abraham, T. Murtola, R. Schulz, S. Páll, J. C. Smith, B. Hess and E. Lindahl, GROMACS: High performance molecular simulations through multi-level parallelism from laptops to supercomputers, *SoftwareX*, 2015, **1**, 19–25.

75 W. Humphrey, A. Dalke and K. Schulten, VMD: visual molecular dynamics, *J. Mol. Graphics*, 1996, **14**(1), 33–38.

This journal is © The Royal Society of Chemistry 2021

Environ. Sci.: Nano, 2021, **8**, 2006–2018 | **2017**

76 D. W. Schaefer, T. Rieker, M. Agamalian, J. S. Lin, D. Fischer, S. Sukumaran, C. Chen, G. Beaucage, C. Herd and J. Ivie, Multilevel structure of reinforcing silica and carbon, *J. Appl. Crystallogr.*, 2000, **33**, 587–591.

77 P. Fratzl, Small-angle scattering in materials science-a short review of applications in alloys, ceramics and composite materials, *J. Appl. Crystallogr.*, 2003, **36**(3), 397–404.

78 C. T. Kresge, M. E. Leonowicz, W. J. Roth, J. C. Vartuli and J. S. Beck, Ordered mesoporous molecular sieves synthesized by a liquid-crystal template mechanism, *Nature*, 1992, **359**(6397), 710–712.

79 W. S. Chiang, E. Fratini, P. Baglioni, D. Georgi, J. H. Chen and Y. Liu, Methane adsorption in model mesoporous material, SBA-15, studied by small-angle neutron scattering, *J. Phys. Chem. C*, 2016, **120**(8), 4354–4363.

80 W. S. Chiang, E. Fratini, P. Baglioni, J. H. Chen and Y. Liu, Pore size effect on methane adsorption in mesoporous silica materials studied by small-angle neutron scattering, *Langmuir*, 2016, **32**(35), 8849–8857.

81 M. Doucet, J. H. Cho, G. Alina, J. Bakker, W. Bouwman, P. Butler and A. Washington, *SasView Version 4.1*, Zenodo, 2017.

82 S. Kallus, A. Hahn and J. D. F. Ramsay, Gas adsorption in MCM-41 porous silicas dynamic measurements using SANS, *Eur. Phys. J. E: Soft Matter Biol. Phys.*, 2003, **12**(1), 31–33.

83 Y. B. Melnichenko, G. D. Wignall, D. R. Cole and H. Frielinghaus, Adsorption of supercritical CO_2 in aerogels as studied by small-angle neutron scattering and neutron transmission techniques, *J. Chem. Phys.*, 2006, **124**(20), 204711.

84 C. I. Merzbacher, J. G. Barker, K. E. Swider, J. V. Ryan, R. A. Bernstein and D. R. Rolison, Characterization of multi-phase aerogels by contrast-matching SANS, *J. Non-Cryst. Solids*, 1998, **225**, 234–238.

85 H. Sun, H. Zhao, N. Qi, X. Qi, K. Zhang, W. Sun and Y. Li, Mechanistic insight into the displacement of CH_4 by CO_2 in calcite slit nanopores: the effect of competitive adsorption, *RSC Adv.*, 2016, **6**(106), 104456–104462.

86 H. Sun, H. Zhao, N. Qi and Y. Li, Simulation to enhance shale gas recovery using carbon dioxide in silica nanopores with different sizes, *Energy Technol.*, 2017, **5**(11), 2065–2071.

87 P. He, H. Liu, J. Zhu, Y. Li, S. Huang, P. Wang and H. Tian, Tests of excess entropy scaling laws for diffusion of methane in silica nanopores, *Chem. Phys. Lett.*, 2012, **535**, 84–90.

88 N. Muroyama, A. Yoshimura, Y. Kubota, K. Miyasaka, T. Ohsuna, R. Ryoo, P. I. Ravikovitch, A. V. Neimark, M. Takata and O. Terasaki, Argon adsorption on MCM-41 mesoporous crystal studied by in situ synchrotron powder X-ray diffraction, *J. Phys. Chem. C*, 2008, **112**(29), 10803–10813.

89 T. Hofmann, D. Wallacher, P. Huber, R. Birringer, K. Knorr, A. Schreiber and G. H. Findenegg, Small-angle x-ray diffraction of Kr in mesoporous silica: Effects of microporosity and surface roughness, *Phys. Rev. B: Condens. Matter Mater. Phys.*, 2005, **72**(6), 064122.

90 A. A. Sizova, Sizov V. V., Brodskaya E. N., Adsorption of CO_2/CH_4 and CO_2/N_2 mixtures in SBA-15 and CMK-5 in the presence of water: A computer simulation study, *Colloids Surf., A*, 2015, **474**, 76–84.

91 Y. Belmabkhout and A. Sayari, Adsorption of CO_2 from dry gases on MCM-41 silica at ambient temperature and high pressure. 2: Adsorption of CO_2/N_2, CO_2/CH_4 and CO_2/H_2 binary mixtures, *Chem. Eng. Sci.*, 2009, **64**, 3729–3735.

92 T. Steiner, The hydrogen bond in the solid state, *Angew. Chem., Int. Ed.*, 2002, **41**(1), 48–76.

2018 | *Environ. Sci.: Nano*, 2021, **8**, 2006–2018

This journal is © The Royal Society of Chemistry 2021